LETTER

https://doi.org/10.1038/s41586-018-0474-7

Three-dimensional printing of hierarchical liquid-crystal-polymer structures

Silvan Gantenbein[1], Kunal Masania[1]*, Wilhelm Woigk[1], Jens P. W. Sesseg[2], Theo A. Tervoort[2]* & André R. Studart[1]*

Fibre-reinforced polymer structures are often used when stiff lightweight materials are required, such as in aircraft, vehicles and biomedical implants. Despite their very high stiffness and strength[1], such lightweight materials require energy- and labour-intensive fabrication processes[2], exhibit typically brittle fracture and are difficult to shape and recycle[3,4]. This is in stark contrast to lightweight biological materials such as bone, silk and wood, which form by directed self-assembly into complex, hierarchically structured shapes with outstanding mechanical properties[5–11], and are circularly integrated into the environment. Here we demonstrate a three-dimensional (3D) printing approach to generate recyclable lightweight structures with hierarchical architectures, complex geometries and unprecedented stiffness and toughness. Their features arise from the self-assembly of liquid-crystal polymer molecules into highly oriented domains during extrusion of the molten feedstock material. By orienting the molecular domains with the print path, we are able to reinforce the polymer structure according to the expected mechanical stresses, leading to stiffness, strength and toughness that outperform state-of-the-art 3D-printed polymers by an order of magnitude and are comparable with the highest-performance lightweight composites[1,12]. The ability to combine the top-down shaping freedom of 3D printing with bottom-up molecular control over polymer orientation opens up the possibility to freely design and realize structures without the typical restrictions of current manufacturing processes.

The manufacture of polymer-based lightweight structures is currently limited either to 3D-printed complex parts, which show poor molecular orientation and mechanical strength[13,14] (Extended Data Fig. 1), or to highly oriented stiff polymers, the shapes of which are restricted to simple geometries[15,16]. To combine shaping freedom with molecular orientation, the 3D printing of liquid-crystal elastomers has been recently exploited[17–19]. Although desirable shape-morphing effects can be achieved, the Young's modulus of such soft elastomers is three to four orders of magnitude lower than those of high-performance liquid-crystal synthetic fibres. This is explained by the presence of relatively long, flexible segments in the molecular structure of the polymer.

To fully exploit the shaping freedom of 3D printing and the favourable mechanical properties expected from molecularly oriented liquid-crystal polymers (LCPs), we propose an approach that conceptually follows two design principles that are used in nature to grow strong and tough biological materials[20]. First, anisotropy is achieved during the printing process by self-assembly of the LCP along the print path. Second, anisotropy and the complex-shaping capabilities offered by 3D printing are exploited to tailor the local stiffness and strength of the structure according to the specific loading conditions imposed by the environment.

The rigid molecular segments of aromatic thermotropic polyesters are known to self-assemble into nematic domains at temperatures higher than the melting temperature of the material (Fig. 1a, b). In the polymer melt at rest, there is no preferred orientation of the individual ordered nematic domains, leading to a globally random orientation distribution (Fig. 1c). Extrusion of the polymer melt through the nozzle of the 3D printer gives rise to shear and extensional flow fields that align the nematic domains in the direction of flow (Fig. 1d). As the molten polymer exits the nozzle, the flow ceases and the extruded filament is exposed to the ambient temperature. A temperature gradient is then formed between the cold surface of the filament and its hot interior. Rapid cooling at the surface leads to solidification of the nematic order in the flow-aligned arrangement. By contrast, polymer chains present in the interior of the filament experience slower cooling, and therefore have sufficient time to re-orient, driven by thermal motion. As a result, the extruded filaments possess a core–shell structure, in which a highly aligned skin encloses a less oriented core (Figs. 1e, f, 2a). The thickness of the skin depends on the filament diameter and the operating temperatures. A simple analytical heat-transfer model was used to predict the effect of these relevant printing parameters on the final core–shell architecture (Fig. 2b and equation (16) in Methods). Optical microscopy and X-ray scattering experiments confirm the formation of a highly aligned skin, the relative fraction of which increases as the filament size decreases (Fig. 2b–d, Extended Data Fig. 2). Although the possibility of aligning thermotropic LCPs in the nozzle of a fused deposition modelling (FDM) printer has been suggested previously, the mechanical properties of the obtained objects remained below those of their conventional injection-moulded counterparts[21]. By contrast, the core–shell filaments produced in our study showed notable mechanical strength and elastic modulus (Fig. 2).

The effect of the core–shell architecture on the tensile mechanical behaviour of individual filaments was investigated in order to establish a quantitative correlation between mechanical performance and relevant printing parameters. Individual filaments can be extruded vertically starting from the build platform, or horizontally onto the substrate at a constant height. The vertically extruded filament cools symmetrically in air and its diameter is controlled by the diameter of the nozzle (Fig. 1e). During the deposition of horizontal filaments, inhomogeneous heat-transfer conditions at the boundary of the filament and the substrate result in non-uniform skin thickness in the filament cross-section (Fig. 1f). Regardless of the printing configuration, the Young's modulus of the printed filaments increases as much as threefold when the nozzle diameter is decreased from 800 μm to 150 μm, and as much as sevenfold when the layer height is decreased from 400 μm to 50 μm (Fig. 2e, f). A similar trend was observed for the tensile strength of the filaments. This can be qualitatively explained by the increase in the relative fraction of aligned molecules as the filament diameter or layer height decreases. For vertical filaments, the dependence of the Young's modulus on the nozzle diameter is well described by a simple scaling law that is derived from the heat-transfer model used to predict the thickness of the skin layer (equation (16) in Methods). According to this model, the Young's modulus (E) scales with the inverse of the nozzle diameter ($1/d_N$). The ability to produce filaments thinner than the nozzle diameter and thus increase considerably the fraction of aligned domains (Fig. 2c) makes the horizontal

[1]Complex Materials, Department of Materials, ETH Zürich, Zürich, Switzerland. [2]Soft Materials, Department of Materials, ETH Zürich, Zürich, Switzerland. *e-mail: kunal.masania@mat.ethz.ch; theo.tervoort@mat.ethz.ch; andre.studart@mat.ethz.ch

© 2018 Springer Nature Limited. All rights reserved.

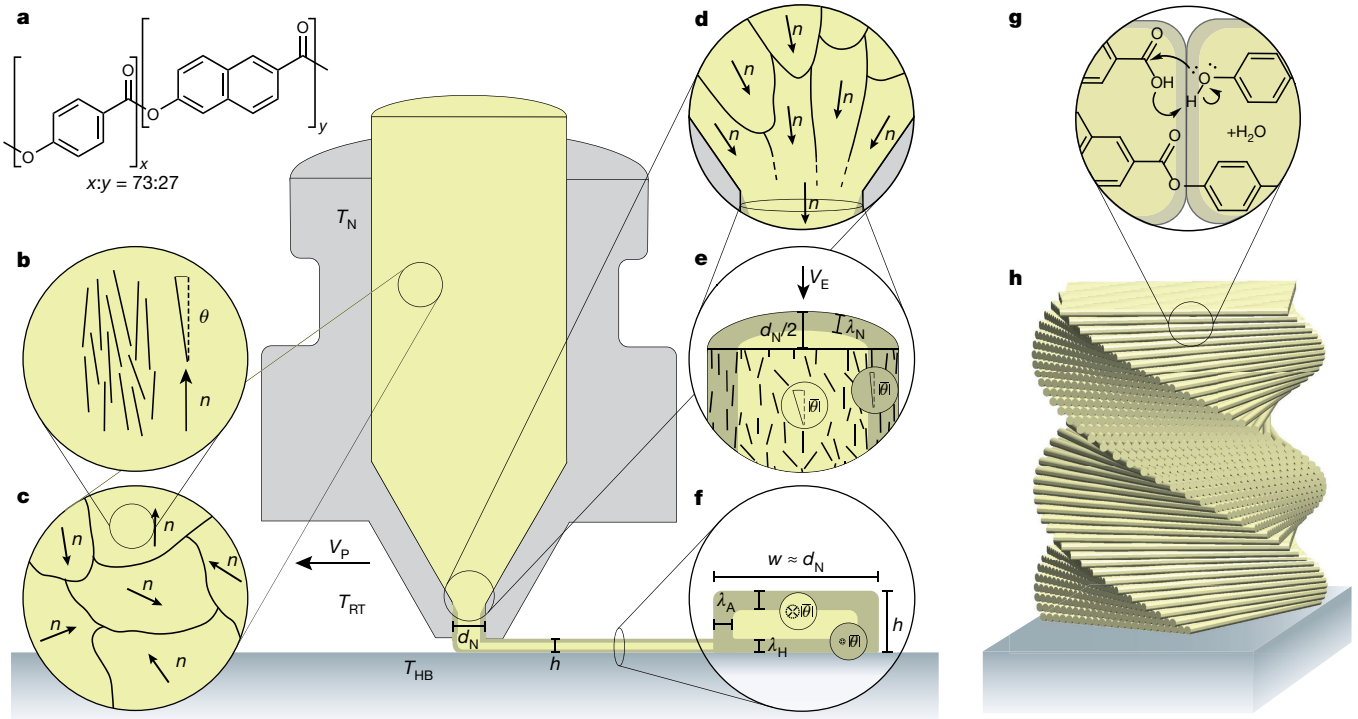

Fig. 1 | Printing hierarchical, thermotropic LCPs using fused deposition modelling. a, An aromatic random copolyester consisting of the rigid monomers *p*-hydroxybenzoic acid and 2-hydroxy-6-naphthoic acid forms short rod-like polymer chains. **b**, The rigid polymer rods align along the same director ***n*** in the melt. They are not perfectly oriented but show a certain misalignment θ towards the director, forming a nematically ordered domain. **c**, Locally aligned nematic domains with randomly oriented directors form the quasi-isotropic bulk of the polymer. **d**, The directors are subjected to elongational and shear forces during the extrusion through the heated nozzle (at temperature T_N) with diameter d_N. These forces can rearrange the polymers in the melt and align the directors along the extrusion direction. **e**, The material starts to lose its orientation once it has been extruded. At the same time the solidification front freezes the nematic order in place, starting from the surface. These two effects result in a core–shell microstructure with a highly aligned shell of thickness λ_N. **f**, Depositing material on a surface at a height h promotes further alignment of the director in the print direction and forms a core–shell structure with different skin thicknesses due to the distinct cooling rates for air, the glass surface and the polymer substrate. T_{HB}, temperature of the heated bed or substrate; T_{RT}, temperature of the environment (room temperature); V_E, velocity of extrusion; V_P printing velocity; w, print width; λ_A, thickness of skin aligned towards air; λ_H, thickness of skin aligned towards the heated bed or substrate. **g**, **h**, After printing, chain ends can chemically crosslink via thermal annealing, which increases the molecular weight and enhances stress transfer between filaments.

printing configuration very effective for improving the stiffness and the strength of the printed materials.

In addition to the nozzle diameter and layer height, temperature is another parameter that can be controlled conveniently during the printing process. Our experimental data show that both the Young's modulus and the tensile strength of printed filaments increase as the temperature at the nozzle is decreased. This correlation can be qualitatively explained by the fact that the solidification process is faster if the nozzle temperature is closer to the melting temperature of the polymer. Faster solidification results in thicker skins and therefore improved stiffness and strength. This effect can also be quantitatively illustrated using the scaling law obtained from the analytical heat-transfer model (Fig. 2g and equation (16) in Methods).

An important additional feature of the aromatic polyester used as the liquid-crystal feedstock is that its printed filaments can be chemically cross-linked by thermal annealing. Cross-linking occurs via post-condensation reactions between carboxylic acid and hydroxy groups present at the end of the macromolecules (Fig. 1g). The formation of cross-links is expected to increase the molecular weight and enhance stress transfer between adjacent macromolecules, thereby improving the tensile behaviour of the polymer under load. Indeed, annealing for 96 h was found to increase the tensile strength of printed filaments by a factor of two, reaching a value of 1 GPa for filaments printed horizontally. Within the first 10 h of thermal treatment, the tensile strength of the filament was observed to follow a square-root dependence on the annealing time. This suggests that the cross-linking reaction is controlled by the diffusion of reaction products—such as water molecules—away from the reaction sites, which supports the hypothesis that a post-condensation reaction is responsible for the observed strengthening effect (Extended Data Fig. 3a).

After analysing the structure and properties of individual filaments, we then turned our attention to more complex fibre laminates that are obtained by printing filaments adjacent to one another in a specific direction (Fig. 3). As expected, maximal Young's modulus and tensile strength are achieved by printing filaments parallel to the mechanical-loading direction (Fig. 3a). Increasing the angle between filament orientation and the loading direction decreases the Young's modulus of the printed structure substantially, as predicted from classical laminate theory (Fig. 3a, Extended Data Fig. 4 and equation (18) in Methods). Overall, the structure, stiffness and strength of the printed laminates can be tuned over a wide range using the same control parameters that were investigated for individual filaments, namely layer height and temperature (Extended Data Fig. 5).

The molecular cross-links formed by thermal annealing also have a considerable effect on the strength of the printed laminates. For low alignment angles (0° and 30°), the bending strength of the laminate increases by 50% to 100% after the thermal treatment (Fig. 3b). Annealed samples tested in tensile mode at 90° also show an almost 100% increase in strength after 96 h (Fig. 3c), while simultaneously increasing the Young's modulus owing to enhanced load transfer between filaments in the composite. The observed strengthening effect follows the diffusion-controlled kinetics that are expected for the post-condensation reaction (Extended Data Fig. 3b). More importantly, thermally induced cross-linking markedly changes the fracture

© 2018 Springer Nature Limited. All rights reserved.

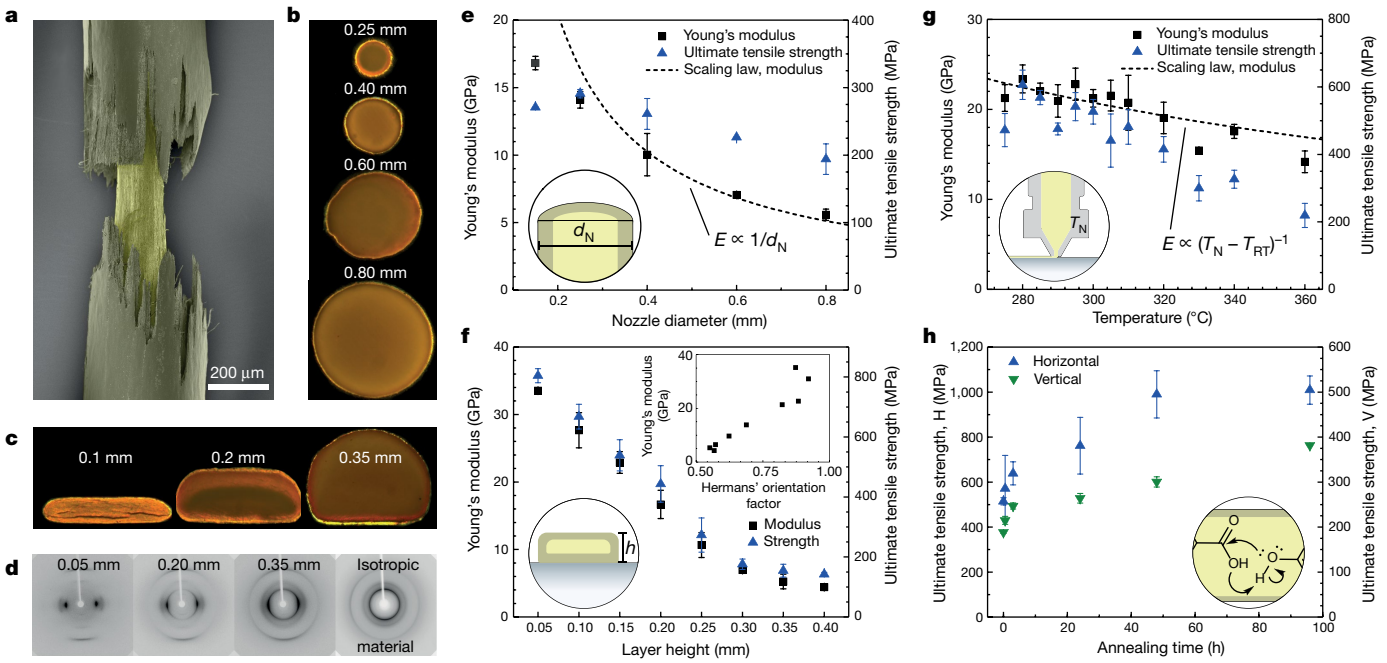

Fig. 2 | The LCP filament properties correlate strongly with the printing conditions. a, False-coloured scanning electron microscopy image of the tensile-tested vertical filament confirms a core–shell structure. The fact that the core of the fibre is still intact indicates that the shell of the LCP fibre is the stiffer phase. **b**, **c**, Polarized light microscopy of a 100-µm cross-section confirms the presence of a core–shell structure in both vertical (**b**) and horizontal (**c**) filaments, as indicated by the more intense illumination of the skin of the printed filaments compared to the core. **d**, X-ray diffraction measurements confirm a higher fraction of oriented polymers in thinner samples. **e**, The Young's modulus and the strength of vertically extruded lines increase with decreasing nozzle diameter because of the increased fraction of oriented polymer in the print line. This hypothesis is supported by a scaling law that successfully captures the dependence of the Young's modulus on the nozzle diameter d_N. **f**, This effect of the core–shell architecture also translates to horizontally printed filaments, where the Young's modulus and strength increase with decreasing print filament height, reaching a maximum reported modulus of 34 GPa and a maximum strength of 800 MPa. **g**, Increased printing temperatures lead to longer cooling times, and therefore longer times for the freezing of the aligned nematic microstructure. This results in an inverse correlation between the Young's modulus and the temperature difference ($T_N - T_{RT}$). **h**, Solid-state annealing further enhances the properties by increasing the molecular weight of the polymer. The strength increases up to 400 MPa for vertically extruded filaments (V) and up to 1 GPa for horizontally printed filaments (H). Error bars indicate the standard deviation for five to ten measurements at each data point.

behaviour of the printed laminates (Fig. 3d). Complete fracture of laminates subjected to annealing is possible only after more than 8% tensile strain is applied. During such straining, multiple peak loads have to be overcome, which leads to substantial energy dissipation during the fracture process. The multiple stress peaks observed resemble those of toughening mechanisms in resilient biological materials such as mollusc shells and bone. This toughening effect contrasts with the abrupt failure of the unannealed specimens after a peak stress is achieved. On the basis of these results and the increased shear strength of the laminates (Extended Data Fig. 6a), we infer that the thermal treatment not only strengthens the individual filaments but also establishes cross-links between filaments in the laminate. Such cross-links are expected to enhance stress transfer between filaments (Extended Data Fig. 6b) and to prevent their delamination through crack-arresting mechanisms. Therefore, the high toughness of the annealed laminates probably emerges from the hierarchical cross-linking of macromolecules and of filaments at increasing length scales.

Besides the self-assembly and hierarchical cross-linking of macromolecules, our 3D printing approach provides a means to replicate other design principles of biological materials. Analogous to the biological growth of living tissues, 3D printing is unique in its ability to create customized material architectures in a layer-by-layer additive fashion. We illustrate this capability by 3D-printing laminate architectures in which the filament orientation is designed to best respond to the local strains imposed by a specific mechanical loading condition. In our example, a plate with a central hole is subjected to a global tensile strain in one specific direction (Fig. 4a). Two distinct laminate architectures containing either straight (unidirectional) or curvilinear (directional) filaments (Extended Data Fig. 7) were tested and compared to a reference sample that comprised isotropic hot-pressed LCPs. The higher intrinsic strength and stiffness of printed filaments leads to a threefold increase in stiffness and a fivefold increase in strength of the unidirectional architecture compared to isotropic LCPs. The use of a load-specific print architecture that follows the stress lines that develop around the hole doubles the strength of the sample compared to the unidirectional sample. Thermal annealing further increases the strength and stiffness of both sample geometries.

Laminates with unidirectional and curvilinear designs contain filaments lying predominantly parallel to the loading direction to arrest cracks that propagate from the central hole, which acts as a stress concentrator. The high local strains in the periphery of the hole were experimentally confirmed by strain maps obtained by digital image correlation analysis (Fig. 4b). Similar to the fibre architectures found in wood and bone, the aligned reinforcement of such laminates prevents catastrophic failure by promoting crack-arresting mechanisms within the material as well as providing strength and toughness via the core–shell structure of the printed filament. As a result, the modulus of toughness of laminates with aligned architectures is about 30- to 55-fold higher than that of the isotropic reference specimen. The higher strength and Young's modulus of specimens that display the curvilinear reinforcement design demonstrates our ability to produce high-performance laminates by tuning the fibre orientation to best match the stress lines developed throughout the mechanically loaded structure.

The high toughness of the printed laminates is accompanied by a marked increase in specific Young's modulus without loss of the intrinsically high damping properties of aromatic polyesters (Fig. 4c). With this unique combination of properties, our printed LCP laminates clearly stand out in comparison to other existing lightweight materials. In terms of specific strength and Young's modulus, printed LCPs surpass the properties of glass fibre-reinforced polymers and

© 2018 Springer Nature Limited. All rights reserved.

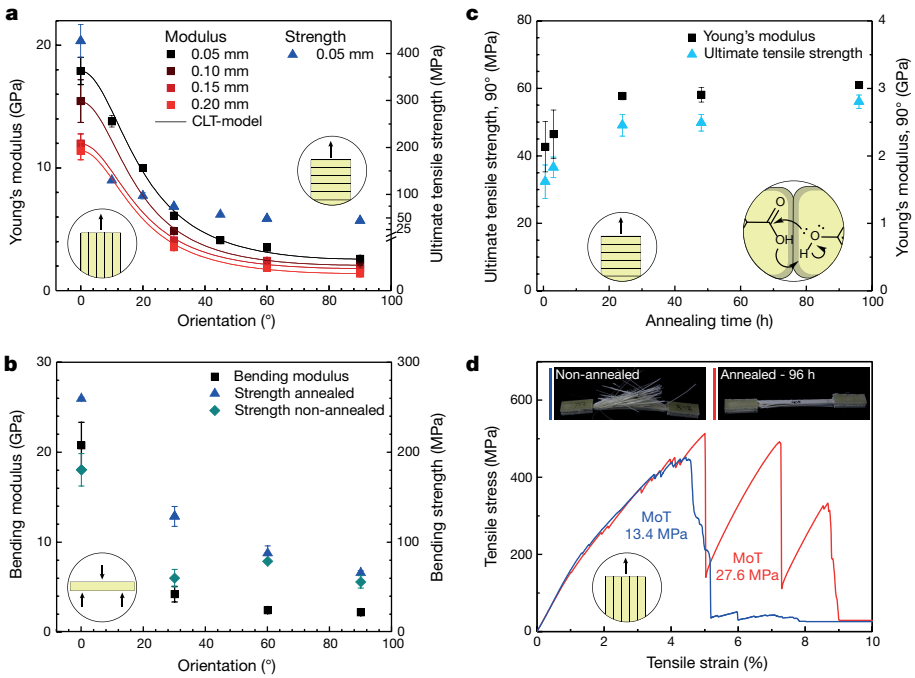

Fig. 3 | Mechanical properties of LCP parts printed through the unidirectional deposition of filaments. a, Like that of fibre-reinforced composite materials, the Young's modulus of unidirectional printed parts depends on the printing orientation, as predicted by classical laminate theory (CLT). **b**, Bending properties follow the same trend, as expected for a system composed of oriented fibres. Annealing increases the bending strength by increasing the stress transfer between different print filaments. **c**, Annealing tensile samples printed 90° to the loading direction increases the strength over time owing to the improved adhesion between filaments. Initially, this process is controlled by the diffusion of water molecules generated during the post-condensation reaction. Error bars indicate the standard deviation for five to ten measurements at each data point. **d**, For samples with print lines oriented in the loading direction, the fracture mode changes from a broom-like to a tough layer-like fracture owing to the improved filament adhesion achieved by thermal annealing (96 h). This change also results in a saw-tooth break pattern in the stress–strain curve, which increases the amount of energy required to fracture the part (modulus of toughness, MoT) by a factor of two.

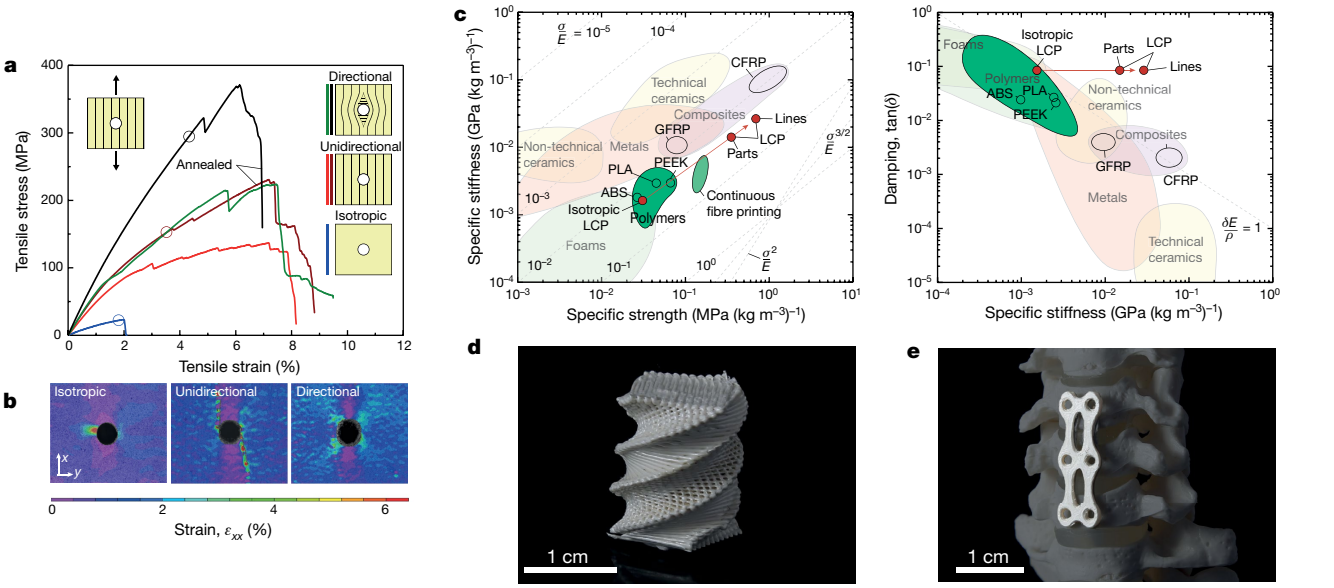

Fig. 4 | Mechanical properties and complex geometry of 3D-printed LCP laminates and parts. a, Mechanical response under tension of open-hole LCP laminates, highlighting the improved properties obtained when the filament architecture is designed to follow the stress lines developed within the loaded material. **b**, Open-hole strain maps measured by digital image correlation just before fracture. **c**, Ashby diagrams indicating the specific stiffness and specific strength (left) and damping (right) properties of LCP lines and parts compared to the isotropic counterpart and state-of-the-art polymers and reinforced composite materials[22]. σ, strength; ρ, density; ABS, acrylonitrile butadiene styrene; CFRP, carbon fibre reinforced polymer; GFRP, glass fibre reinforced polymer; PEEK, polyether ether ketone; PLA, polylactic acid. **d**, **e**, Examples of 3D-printed LCP parts with complex fibre architectures and geometries: impact-resistant Bouligand-type structure with twisted plywood arrangement of printed fibres (**d**) and biomedical implant with a local bearing enhancement where the print lines are programmed to follow the principle stress direction around holes (**e**).

© 2018 Springer Nature Limited. All rights reserved.

continuous fibre-printed composites (Fig. 4c). Indeed, the stiffness and strength of our printed laminates approach those of carbon-fibre reinforced polymers, with the added value of recyclability (Extended Data Fig. 8), automated manufacturing and lower carbon footprint. By taking advantage of the shaping capabilities of 3D printing, special complex geometries and application-specific shapes can be produced using the proposed additive technology (Fig. 4d, e). By combining the tool path control provided by the 3D printer with the tunable orientation of self-assembled building blocks within the ink, we can reach unparalleled levels of hierarchical structural complexity (Fig. 4d). As opposed to current FDM printed polymer parts, the anisotropic filament architectures implemented in these complex geometries can be designed to achieve toughness comparable to that of the strongest polymer-based lightweight materials. This approach is in contrast with the usual strategy to reduce anisotropy in 3D-printed synthetic parts, and opens up the possibility to fabricate structures that can fulfil different performance requirements while ensuring a sustainable circular life cycle of the material.

Online content

Any methods, additional references, Nature Research reporting summaries, source data, statements of data availability and associated accession codes are available at https://doi.org/10.1038/s41586-018-0474-7.

Received: 12 March 2018; Accepted: 19 July 2018;
Published online 12 September 2018.

1. Amacher, R. et al. Thin ply composites: experimental characterization and modeling of size-effects. *Compos. Sci. Technol.* **101**, 121–132 (2014).
2. Witik, R. A., Payet, J., Michaud, V., Ludwig, C. & Månson, J.-A. E. Assessing the life cycle costs and environmental performance of lightweight materials in automobile applications. *Composites, Part A* **42**, 1694–1709 (2011).
3. Kiser, B. Circular economy: Getting the circulation going. *Nature* **531**, 443–446 (2016).
4. Yang, Y. et al. Recycling of composite materials. *Chem. Eng. Process.* **51**, 53–68 (2012).
5. Launey, M. E., Buehler, M. J. & Ritchie, R. O. On the mechanistic origins of toughness in bone. *Ann. Rev. Mater. Res.* **40**, 25–53 (2010).
6. Wegst, U. G. K., Bai, H., Saiz, E., Tomsia, A. P. & Ritchie, R. O. Bioinspired structural materials. *Nat. Mater.* **14**, 23–36 (2015).
7. Meyers, M. A., Chen, P. Y., Lin, A. Y. M. & Seki, Y. Biological materials: Structure and mechanical properties. *Prog. Mater. Sci.* **53**, 1–206 (2008).
8. Burgert, I. Exploring the micromechanical design of plant cell walls. *Am. J. Bot.* **93**, 1391–1401 (2006).
9. Cranford, S. W., Tarakanova, A., Pugno, N. M. & Buehler, M. J. Nonlinear material behaviour of spider silk yields robust webs. *Nature* **482**, 72–76 (2012).
10. Vollrath, F. & Knight, D. P. Liquid crystalline spinning of spider silk. *Nature* **410**, 541–548 (2001).
11. Smith, B. L. et al. Molecular mechanistic origin of the toughness of natural adhesives, fibres and composites. *Nature* **399**, 761–763 (1999).
12. Grossman, M. et al. Mineral nano-interconnectivity stiffens and toughens nacre-like composite materials. *Adv. Mater.* **29**, 1605039 (2017).
13. Ahn, S. H., Montero, M., Odell, D., Roundy, S. & Wright, P. K. Anisotropic material properties of fused deposition modeling ABS. *Rapid Prototyping J.* **8**, 248–257 (2002).
14. Ning, F., Cong, W., Qiu, J., Wei, J. & Wang, S. Additive manufacturing of carbon fiber reinforced thermoplastic composites using fused deposition modeling. *Composites, Part B* **80**, 369–378 (2015).
15. Lefèvre, J. et al. "Foil spintrusion" of high-performance polymer films. *J. Polym. Sci. B* **50**, 1713–1727 (2012).
16. Schaller, R., Peijs, T. & Tervoort, T. A. High-performance liquid-crystalline polymer films for monolithic "composites". *Composites, Part A* **81**, 296–304 (2016).
17. Kotikian, A., Truby, R. L., Boley, J. W., White, T. J. & Lewis, J. A. 3D printing of liquid crystal elastomeric actuators with spatially programed nematic order. *Adv. Mater.* **30**, 1–6 (2018).
18. Ambulo, C. P. et al. Four-dimensional printing of liquid crystal elastomers. *ACS Appl. Mater. Interfaces* **9**, 37332–37339 (2017).
19. López-Valdeolivas, M., Liu, D., Broer, D. J. & Sánchez-Somolinos, C. 4D printed actuators with soft-robotic functions. *Macromol. Rapid Commun.* **39**, 1700710 (2018).
20. Fratzl, P. & Weinkamer, R. Nature's hierarchical materials. *Prog. Mater. Sci.* **52**, 1263–1334 (2007).
21. Gray, R. W., Baird, D. G. & Bøhn, J. H. Rapid prototyping journal effects of processing conditions on short TLCP fiber reinforced FDM parts. *Rapid Prototyping J.* **4**, 14–25 (1998).
22. Ashby, M. F. *Material and Process Selection Charts* http://www.grantadesign.com/download/pdf/teaching_resource_books/2-Materials-Charts-2010.pdf (Granta Design, 2010).

Acknowledgements We thank G. Ghazaryan and the Kunststoff Ausbildungs- und Technologie-Zentrum for support with filament extrusion, the D-MATL X-ray Platform for access to the diffractometer, and J. Vermant, K. Feldman and N. Bahamonde for discussions. The Swiss Competence Center for Energy Research (SCCER - Capacity Area A3: Minimization of Energy Demand), ETH Foundation grant SP-MaP 01-15, SNSF Project 200021_156011 and consolidator grant BSCGIO_157696 are acknowledged for supporting this research.

Author contributions T.A.T. and A.R.S. conceived the idea together with S.G. and K.M.; S.G., W.W., K.M. and J.S. carried out the experimental work; S.G., K.M., W.W., T.A.T. and A.R.S. carried out the analysis and co-wrote the paper.

Competing interests The authors have filed patent application EP18179376 relating to this work.

Additional information
Extended data is available for this paper at https://doi.org/10.1038/s41586-018-0474-7.
Reprints and permissions information is available at http://www.nature.com/reprints.
Correspondence and requests for materials should be addressed to K.M., T.A.T. or A.R.S.
Publisher's note: Springer Nature remains neutral with regard to jurisdictional claims in published maps and institutional affiliations.

© 2018 Springer Nature Limited. All rights reserved.

METHODS

Preparation of LCP filament. LCP (Vectra A950, Ticona) was dried at 150 °C for 12 h before extrusion. LCP filaments were prepared using a single-screw extruder (Teach-Line E20 T, Collin) that was heated to 280, 290, 290 and 260 °C at the four zones along its longitudinal axis. The filament was extruded at 60 r.p.m., cooled in a water bath (Teach-Line WB850, Collin) and collected on a modified flat film line (Teach-Line CR72 T, Collin). The speed of the collector rolls was adjusted to achieve a filament diameter of 1.75 mm. The filament was wound on FDM spools and dried at 70 °C for at least 24 h before use. Because flow-induced molecular orientation is a well-established phenomenon for liquid-crystal systems[23–27], the proposed printing technology should be applicable to a broad range of LCPs beyond the polyester used in this study.

FDM printing setup. A commercially available FDM printer (Ultimaker 2+, Ultimaker) was modified with a geared direct drive extruder and an all-metal V6 hotend (E3D) to achieve temperatures up to 400 °C (Extended Data Fig. 9). The borosilicate glass build-plate was heated to 90 °C and coated with a thin layer of PVA-based adhesive spray (3DLac) before printing with LCP to improve bed adhesion and reduce warping. Generally, parts were printed at 295 °C at a speed of 35 mm s^{-1} with part cooling fans running at 20%. For printing lines, the speed was reduced to 20 mm s^{-1} to improve the quality of lines in contact with the glass surface.

PLA and PEEK reference samples were printed using commercial filaments (Dutch Filaments B.V. and 3D4MAKERS) at a temperature of 210 °C and 380 °C, respectively. The build-plate was heated to 60 °C for PLA and 120 °C for PEEK. All other parameters were kept the same as for printing LCP. PEEK samples were further heat-treated after printing at 150 °C for one hour followed by one hour at 200 °C to reach optimum crystallization.

Print paths (Gcode) with reduced control over the print directions were generated with Cura, an open-source FDM slicer from Ultimaker. A custom slicer using Grasshopper for Rhinoceros (McNeel) was developed for objects with spatially tuned directional print paths or those for which the orientation of the print path was important.

Thermal annealing. The solid-state thermal annealing was performed by heating the samples to 270 °C under constant nitrogen flow for 0 h to 96 h. Solid-state cross-linking occurs via post-condensation reactions between carboxylic acid and hydroxy groups[28] of the printed samples. The samples were fixed on a steel plate with polyimide tape to prevent deformation during the annealing process.

Tensile tests of printed filaments. Tensile tests were performed on filaments printed vertically starting on the surface and moving upwards (z direction) and horizontally on the glass surface. To produce vertical filaments that do not curl during free-form extrusion, the feedstock material was first printed horizontally to ensure good attachment to the substrate. Vertical and horizontal filaments were printed with varying nozzle diameter and distance to the surface, respectively. Furthermore, the effects of the nozzle temperature and annealing time were examined for both printing configurations.

The filament samples were glued onto individual paper frames to assure a constant gauge length of 20 mm. The tensile tests were carried out at a rate of 2 mm min^{-1} using an AGS-X (Shimadzu) universal testing machine with a 1-kN capacity load cell. Five to ten samples were tested for each batch. The samples were imaged with an optical stereo microscope (WILD M10, Leica) during testing and their width and thickness measured using Fiji image analysis[29]. Data analysis was performed using a custom MATLAB script.

X-ray diffraction of printed filaments. The X-ray diffraction patterns of printed filaments with different diameters (vertical) and layer heights (horizontal) were measured on a single crystal diffractometer (Xcalibur PX, Oxford Diffraction). A molybdenum (Mo-Kα) X-ray source was used with a graphite monochromator. The samples were mounted with the director axis perpendicular to the incident X-ray beam and the scattering was detected on an Onyx CCD detector. Azimuthal angle intensity distribution $I(\phi)$ scans at $2\theta \approx 9°$ were analysed using the CrysAlisPro 171.36.20 software and the Hermans' orientation factor[30] f was calculated using the following equation:

$$f = 1 - 3\langle \cos^2\phi \rangle \quad (1)$$

$$\langle \cos^2\phi \rangle = \frac{\int I(\phi)\sin\phi\cos^2\phi \mathrm{d}\phi}{\int I(\phi)\sin\phi \mathrm{d}\phi} \quad (2)$$

Optical microscopy of printed filaments. Printed filament samples were embedded perpendicular to the print or extrusion direction using optically transparent epoxy Araldite 2020 (Huntsman) and were polished with a laboratory polishing machine (labopol-21, Struers). Polishing was carried out using progressively finer grades of emery paper at intervals of 240, 800, 1,200, 2,400 and 4,000 grit followed by 1 μm and 0.25 μm diamond pastes. The samples were then mounted on standard glass slides using the optically transparent epoxy and, finally, ground and polished to a nominal thickness of 100 μm. An AXIO Scope (Zeiss) optical microscope was used to image the cross-section of the samples using dark-field cross-polarized transmitted light.

Scanning electron microscopy of printed filaments. Printed filaments were imaged after breakage using a scanning electron microscope (Leo 1530 Gemini, Zeiss) operated with an acceleration voltage of 3 kV. Before imaging, the samples were coated with a 5 nm platinum layer using a compact coating unit (CCU-010, Safematic).

Tensile tests of printed parts. Tensile tests were carried out using a Z020 (Zwick) universal testing machine with a 20 kN capacity load cell. Unidirectional tensile test specimens (ISO 527-5) with a nominal width of 5 mm, length of 110 mm and thickness of 2 mm were printed with print-filament orientation varying from 0° to 90° with respect to the testing direction. The samples were supported in the clamping region with bonded glass fibre end tabs, resulting in a gauge length of 65 mm. Specimens were tested at a displacement rate of 2 mm min^{-1} and data was acquired for a minimum of five samples. Data analysis was performed using a custom MATLAB script. In addition to the print direction, the effects of different layer heights, temperatures, and annealing time were investigated. Additional data for the Ashby diagram in Fig. 4c were taken from the literature[1,31–35] or from https://www.carbon3d.com/materials/, or as the bulk value when data was not available.

Bending tests of printed parts. Bending tests were carried out on an AGS-X (Shimadzu) universal testing machine with a three-point bending setup using a span of 24 mm (ASTM D790M). Five repeats for samples with different thicknesses (layer heights) were measured before and after annealing at a displacement rate of 2 mm min^{-1}.

Dynamic mechanical analysis. Dynamic mechanical analysis measurements were performed on a Q800 (TA Instruments) instrument using a three-point bending set up with a 20-mm span. The printed LCP samples were 2 mm thick, 5 mm wide and 30 mm long with a 0° orientation along the span. A pre-load of 0.05 N was applied before the measurement. The displacement amplitude was set to 40 μm and the frequency was held at 100 Hz. Three samples were measured at a constant temperature of 30 °C. Five samples of the isotropic and unidirectional orientation were measured. The complex modulus E^* consisting of the storage modulus E', the loss modulus E'' and loss factor, $\tan\delta$, were measured.

Open-hole tensile test. Open-hole tensile (OHT) tests were performed on a Z020 (Zwick) universal testing machine with a 20-kN-capacity load cell. The OHT specimens had a width of 35 mm and a width-to-hole diameter ratio of 6 (ASTM D5766). Tests were conducted in accordance to the standard ISO 527. Five samples of each batch were clamped in hydraulic gripers with a clamping pressure of 5 bar and were tested in tension with a controlled displacement rate of 2 mm min^{-1}.

Video gauge and digital image correlation. The Poisson's ratio of printed LCP parts was determined by calculating the negative ratio of the transverse and longitudinal strains. Both strain components were measured simultaneously on unidirectional tensile specimens using a video gauge tracking. Optical extensometers were positioned using the Vic-Gauge software (Correlated Solutions).

The shear properties were measured on uniaxial tensile specimens with a ±45° balanced and symmetric laminate (ASTM D3518) for five repeats per batch. The shear strain was calculated as the difference between the longitudinal strain and the transverse strain of the laminate. The global strains were measured optically during the test with virtual extensometers using the Vic-Gauge software. The shear stress was calculated as the ratio of the applied load and twice the cross-sectional area of the specimen, whereas the in-plane shear strength was obtained from the applied load at failure. The in-plane shear modulus of the unidirectional lamina was obtained from the initial slope of the stress–strain curve over a strain range of 0.1%–0.5%.

Digital image correlation was used to measure the local displacements of the OHT specimens. A 12 MP Prosilica camera (Allied Vision) with an 80-mm focal length lens and a 45-mm extension tube were used to acquire images with a rate of 2 Hz. The analysis of these images was performed using the digital image correlation software Vic-2D 6 (Correlated Solutions). Analyses were carried out with a subset size and step size of 29 and 7, respectively. The software generates two-dimensional displacement fields of the loaded samples in relation to the unloaded position. These fields enable one to investigate the induced in-plane strain components, that is, ε_{xx}, ε_{yy} and γ_{xy}, as a function of the global longitudinal strain. To record the deformation of the sample surface during both tests, a speckle pattern with a dot size of about 50 μm was applied with an acryl colour spray can before testing.

Analytical models for skin formation. Two possible mechanisms may explain the formation of the core–shell architecture of the printed filaments: preferential shear-induced alignment of LCP domains at the walls of the nozzle, or rapid cooling of the filament surface. These distinct scenarios are evaluated and discussed below.

© 2018 Springer Nature Limited. All rights reserved.

Skin formation due to shear at the nozzle wall. The formation of a skin in printed filaments may result from the shear-induced alignment of LCP molecules close to the walls of the nozzle, where shear rates are maximal during extrusion. To evaluate this hypothesis, we first estimate the thickness of such a shear-induced skin layer (λ) for different nozzle diameters (d_N). Because the skin thickness directly affects the Young's modulus of the filaments, this theoretical analysis is later compared with our experimental mechanical data to test the hypothesis.

The thickness of the skin layer depends on the shear rate profile across the radius of the nozzle. For fully developed laminar flow, the shear rate is zero at the centre of the nozzle ($r=0$) and increases continuously until it reaches the maximal value at the wall ($r=R$). Because the time required for alignment increases for lower shear rates, there will be a critical radius r_c above which the shear rates will be sufficiently high ($\dot{\gamma} > \dot{\gamma}_c$) to align the particles within the residence time of the material in the nozzle. Such a critical radius defines the skin thickness as $\lambda = R - r_c$.

To establish a correlation between λ and d_N ($2R$) we compare the time required for alignment (t_a) with the residence time (t_{res}). For an anisotropic rod-like particle suspended in a fluid, the alignment time should scale with the inverse of the shear rate, such that:

$$t \approx \frac{1}{\dot{\gamma}} \tag{3}$$

As a first approximation, we assume this simple relation to also be applicable to the LCP polymers investigated here. It follows that $t_a \approx 1/\dot{\gamma}_c$. To determine $\dot{\gamma}_c$ and thus t_a, we estimate the shear rate profile along the radius of the nozzle ($\dot{\gamma}(r)$).

The shear rate profile can be calculated from the derivative of the flow velocity with respect to the nozzle radius ($v(r)$). Such flow velocity depends on the rheological properties of the fluid. For a non-Newtonian fluid, the velocity profile is given by:

$$v(r) = \frac{3n+1}{n+1}\frac{Q}{\pi R^2}\left[1 - \left(\frac{r}{R}\right)^{1+1/n}\right] \tag{4}$$

where Q is the volumetric flow rate. Here, we assume the fluid to be described by a power-law relation, such that the viscosity (η) is given by $\eta = k\dot{\gamma}^{n-1}$, where k and n are constants. By taking the derivative of the velocity profile, the shear rate at different radial positions can be directly obtained:

$$|\dot{\gamma}(r)| = \frac{3n+1}{n}\frac{Q}{\pi R^3}\left(\frac{r}{R}\right)^{1/n} \tag{5}$$

Combining equations (3) and (5) leads to the following scaling relation for the alignment time as a function of the nozzle radius:

$$t_a \approx \frac{n}{3n+1}\frac{\pi R^3}{Q}\left(\frac{r_c}{R}\right)^{-1/n} \tag{6}$$

Comparison of the alignment time with the residence time of the material inside the nozzle enables us to predict the amount of material that aligns during the extrusion process. The residence time for a nozzle of length L is given by:

$$t_{res} = \frac{\pi R^2 L}{Q} \tag{7}$$

As shear-induced alignment occurs when $t \leq t_{res}$, equations (6) and (7) can be combined to obtain:

$$\lambda = R\left\{1 - cR^n\left[\frac{n}{(3n+1)L}\right]^n\right\} \tag{8}$$

where c is a constant that is independent of the nozzle radius.

For strongly shear-thinning fluids such as the LCP melts, it is reasonable to assume that $n \to 0$. This simplifies equation (8) to $\lambda = R(1-c)$. Combining this relation with the expected Young's modulus ($E_V = \lambda E_{skin}/d_N$, see main text), we finally obtain:

$$E_V = \frac{(1-c)E_{skin}}{2} \tag{9}$$

This relation shows that the elastic modulus of the filament does not dependent on the nozzle diameter under the assumptions outlined above. Because our experimental data show a clear decrease of E_V with increasing nozzle diameters (Fig. 2e), our analysis suggests that skin formation is not controlled by shear-induced alignment at the nozzle wall.

Skin formation due to rapid cooling of the filament surface. Another hypothesis is that the thickness of the filament skin is determined by the cooling kinetics of the extrudate as the material exits the nozzle. This scenario can be theoretically described using a simple heat-transfer model. Such analysis assumes that the LCP nematic domains align strongly during extrusion of the feedstock material through the nozzle and that such alignment is maintained in the filament after extrusion only if the material is cooled fast enough to prevent random reorientation of domains driven by thermal motion. Moreover, the LCP domains in the extruded filament are assumed to reach the same level of orientation within the entire range of extrusion temperatures and filament thicknesses investigated in our experiments (Fig. 2).

The cooling of the filament after it leaves the printing nozzle can be described using the following equation describing the spatio-temporal evolution of the temperature of the material:

$$T(x,t) = T_{RT} + (T_N - T_{RT})\mathrm{erf}\left(\frac{x}{2\sqrt{\alpha t}}\right) \tag{10}$$

where x is the distance from the filament surface, t is the time elapsed after the material exits the nozzle, T_N is the temperature inside the nozzle, T_{RT} is the temperature of the substrate (that is, room temperature) and α is the thermal diffusivity. Using a Taylor series expansion of the error function and considering only the first term, we obtain:

$$T(x,t) = T_{RT} + (T_N - T_{RT})\left(\frac{x}{\sqrt{\pi\alpha t}}\right) \tag{11}$$

This simple equation can be used to predict the fraction of material that solidifies sufficiently fast to maintain the alignment of the LCP domains along the extrusion direction. Solidification requires that the temperature of the extruded material reaches the melting temperature ($T(x,t) = T_m$), whereas the preservation of flow-induced alignment is only possible if the cooling timescale t lies below the relaxation time of the LCP domains (τ). Using the skin depth λ to quantify the fraction of aligned material, we obtain the following relation:

$$\lambda = \frac{T_m - T_{RT}}{T_N - T_{RT}}\sqrt{\pi\alpha\tau} \tag{12}$$

The relaxation time τ provides a characteristic timescale for the exponential decay of the domain orientation parameter S, as described by the equation[36]:

$$S(t) = S_0 \exp\left(-\frac{t}{\tau}\right) \tag{13}$$

where S_0 is the initial flow-induced orientation. Because the orientation decays exponentially with time and minor misalignments are sufficient to strongly reduce the mechanical properties of the filament along the printing direction, we expect that cooling has to occur within timescales $t \ll \tau$ to obtain a filament shell with high mechanical properties.

Assuming that the core–shell structure is indeed controlled by thermal transport across the extrudate and that the mechanical properties of the filament are determined by the fraction of aligned LCP domains, we can use the above model to predict the dependence of the elastic modulus of the LCP filaments on the printing parameters. To this end, we estimate the elastic modulus E of the whole filament using a rule of mixture:

$$E = \phi_{skin}E_{skin} + \phi_{core}E_{core} \approx \phi_{skin}E_{skin} \tag{14}$$

Here E_{skin} is the modulus of the fully aligned polymer and ϕ_{skin} is the volume fraction of aligned material across the filament. ϕ_{skin} for horizontal and vertical filaments of diameter d_N can be geometrically described as:

$$\begin{aligned}\phi_{skin,V} &= \frac{2\lambda}{d_N}\left(2 - \frac{2\lambda}{d_N}\right) \approx \frac{4\lambda}{d_N} \\ \phi_{skin,H} &= 2\lambda\left(\frac{1}{d_N} + \frac{1}{h}\right)\end{aligned} \tag{15}$$

Introducing these relations into the rule-of-mixture equation yields the Young's modulus as a function of print parameters for the vertically and horizontally printed filaments:

$$\begin{aligned}E_V &= \frac{4E_{skin}}{d_N}\sqrt{\pi\alpha\tau}\left(\frac{T_m - T_{RT}}{T_N - T_{RT}}\right) \\ E_H &= \left(\frac{2}{d_N} + \frac{2}{h}\right)E_{skin}\sqrt{\pi\alpha\tau}\left(\frac{T_m - T_{RT}}{T_N - T_{RT}}\right)\end{aligned} \tag{16}$$

© 2018 Springer Nature Limited. All rights reserved.

The experimentally measured Young's modulus of vertical filaments (Fig. 2e, g) was found to indeed scale with $1/d_N$ and $1/(T_N - T_{RT})$, as predicted by the equations proposed above. This supports the hypothesis that the mechanical properties of the filaments are controlled by the cooling kinetics of the extruded material.

This finding has direct implications for the 3D printing of tough LCP parts, because it implies that highly aligned filaments require not only the design of nozzles that promote shear and extensional flow, but also strategies to quickly extract heat from the extruded material. In our work, the shear and extensional flow was always above the critical value that is needed to orient the nematic domains of the LCP in the melt along the extrusion direction. The cooling was effectively achieved by depositing the material very close to the substrate or to the previously deposited (and cooled) polymer layers, such that thin print layers with low thermal diffusion length are obtained.

Classical laminate theory. The elastic modulus of printed LCP parts for distinct mechanical loading directions was theoretically estimated using classical laminate theory. To this end, we use a coordinate system in which direction 1 corresponds to the print direction and direction 2 lies perpendicular to it, both of which are orthogonal to direction 3. On the basis of this coordinate system, the following transformation matrix was applied:

$$\{\sigma\}_{12} = T\{\sigma\}_{xy}$$
$$T = \begin{bmatrix} \cos^2\theta & \sin^2\theta & 2\sin\theta\cos\theta \\ \sin^2\theta & \cos^2\theta & -2\sin\theta\cos\theta \\ -\sin\theta\cos\theta & \sin\theta\cos\theta & \cos^2\theta - \sin^2\theta \end{bmatrix} \quad (17)$$

Using this matrix transformation, the Young's modulus in tensile direction x as a function of the print orientation angle θ can be calculated by the following equation[37]:

$$\frac{1}{E_x} = \frac{\cos^4\theta}{E_{11}} + \frac{\sin^4\theta}{E_{22}} + \left(\frac{1}{G_{12}} - \frac{2\nu_{12}}{E_{11}}\right)\cos^2\theta\sin^2\theta \quad (18)$$

where E_{11} is the Young's modulus in the print direction, E_{22} is the modulus perpendicular to the print direction, G_{12} is the shear modulus and ν_{12} is Poisson's ratio. The material properties that were used for the calculations are listed in Extended Data Table 1 and were calculated from tensile tests.

Code availability. The Grasshopper files for the generation of print paths are available from the corresponding authors on reasonable request.

Data availability. The datasets generated and analysed during this study are available from the corresponding authors on reasonable request. Source Data for Figs. 2–4 and Extended Data Figs. 1–6 and 8 are provided with the online version of the paper.

23. Sarlin, J. & Törmälä, P. Fiber formation and characterization of a thermotropic LCP. *J. Appl. Polym. Sci.* **40**, 453–469 (1990).
24. Chen, B.-K., Tsay, S.-Y. & Chen, J.-Y. Synthesis and properties of liquid crystalline polymers with low T_m and broad mesophase temperature ranges. *Polymer* **46**, 8624–8633 (2005).
25. Crevecoeur, G. & Groeninckx, G. Morphology and mechanical properties of thermoplastic composites containing a thermotropic liquid crystalline polymer. *Polym. Eng. Sci.* **30**, 532–542 (1990).
26. Motamedi, F., Jonas, U., Greiner, A. & Schmidt, H.-W. Preparation and characterization of fibres from a thermotropic liquid crystal polyester with non-coplanar biphenylene units. *Liq. Cryst.* **14**, 959–970 (1993).
27. Rendon, S., Burghardt, W. R. & Bubeck, R. A. Orientation dynamics in commercial thermotropic liquid crystalline polymers in transient shear flows. *Rheol. Acta* **46**, 945–956 (2007).
28. Warner, S. B. & Lee, J. Towards understanding the increase in strength of thermotropic polyesters with heat treatment. *J. Polym. Sci. B* **32**, 1759–1769 (1994).
29. Schindelin, J. et al. Fiji: an open-source platform for biological-image analysis. *Nat. Methods* **9**, 676–682 (2012).
30. Dreher, S. et al. Chain orientation in melt-extruded samples of vectra A, vectra B, and blends in relation to the mechanical properties. *J. Appl. Polym. Sci.* **67**, 531–545 (1998).
31. Dickson, A. N., Barry, J. N., McDonnell, K. A. & Dowling, D. P. Fabrication of continuous carbon, glass and Kevlar fibre reinforced polymer composites using additive manufacturing. *Addit. Manuf.* **16**, 146–152 (2017).
32. Tymrak, B. M., Kreiger, M. & Pearce, J. M. Mechanical properties of components fabricated with open-source 3-D printers under realistic environmental conditions. *Mater. Des.* **58**, 242–246 (2014).
33. Kamthai, S. & Magaraphan, R. Thermal and mechanical properties of polylactic acid (PLA) and bagasse carboxymethyl cellulose (CMCB) composite by adding isosorbide diesters. *AIP Conf. Proc.* **1664**, 060006 (2015).
34. Arivazhagan, A. & Masood, S. Dynamic mechanical properties of ABS material processed by fused deposition modelling. *Int. J. Eng. Res. Appl.* **2**, 2013–2014 (2012).
35. Goyal, R. K., Tiwari, A. N., Mulik, U. P. & Negi, Y. S. Effect of aluminum nitride on thermomechanical properties of high performance PEEK. *Composites, Part A* **38**, 516–524 (2007).
36. Picken, S. J., Aerts, J., Visser, R. & Northolt, M. G. Structure and rheology of aramid solutions: X-ray scattering measurements. *Macromolecules* **23**, 3849–3854 (1990).
37. Gerdeen, J. C. & Rorrer, R. A. L. *Engineering Design with Polymers and Composites* 2nd edn, Ch. 8 (CRC Press, London, 2012).

© 2018 Springer Nature Limited. All rights reserved.

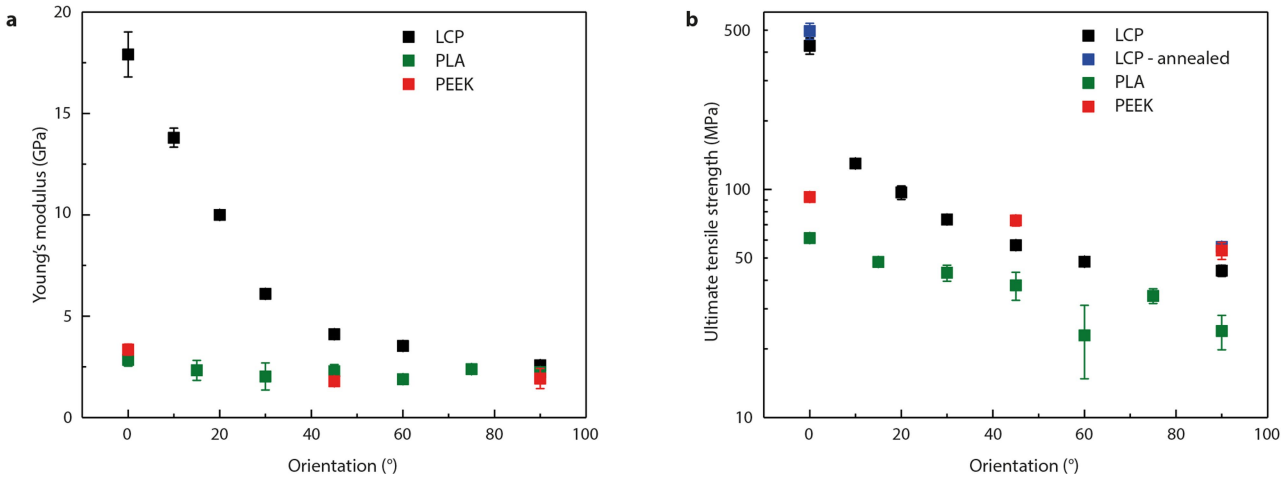

Extended Data Fig. 1 | Comparison between the mechanical properties of different FDM feedstock materials. a, Young's modulus as a function of print orientation for LCP, PLA and PEEK. **b**, Tensile strength of LCP, annealed LCP, PLA and PEEK. The strength of LCP samples is comparable to that of one of the strongest printable polymers (PEEK) at high orientation angles, and to our knowledge surpasses all other tested materials for print orientations below 20°. Error bars indicate the standard deviation for 5–10 measurements at each data point; see Source Data for details.

© 2018 Springer Nature Limited. All rights reserved.

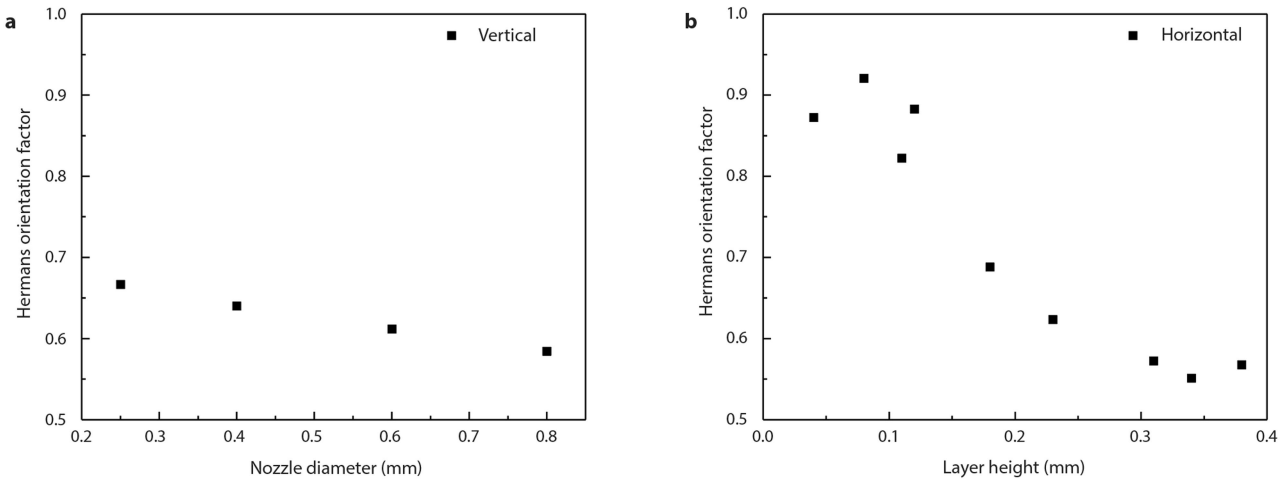

Extended Data Fig. 2 | Values of the Hermans' orientation factor for the LCPs. a, **b**, Hermans' orientation factors as a function of nozzle diameter (**a**) and layer height (**b**). Thinner samples have an increased skin-to-core material ratio and thus a higher orientation factor.

© 2018 Springer Nature Limited. All rights reserved.

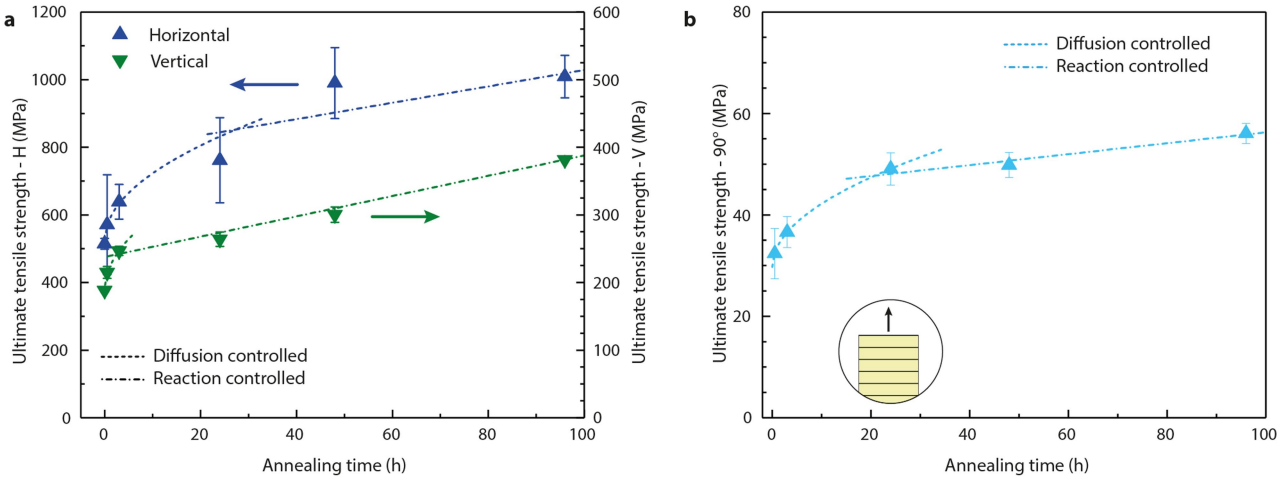

Extended Data Fig. 3 | Effect of annealing time on the ultimate strength of printed LCP filaments and parts. a, Strength (σ) as a function of annealing time (t) for single printed filaments. The experimental data suggest that the reaction is initially controlled by the diffusion of water out of the filament ($\sigma \propto t^{0.5}$) and later on by the intrinsic reaction kinetics ($\sigma \propto t$). **b**, Tensile strength as a function of annealing time for printed parts. The annealing kinetics follow the same trend as in the case of single filaments. Error bars indicate the standard deviation for 5–10 measurements at each data point; see Source Data for details.

© 2018 Springer Nature Limited. All rights reserved.

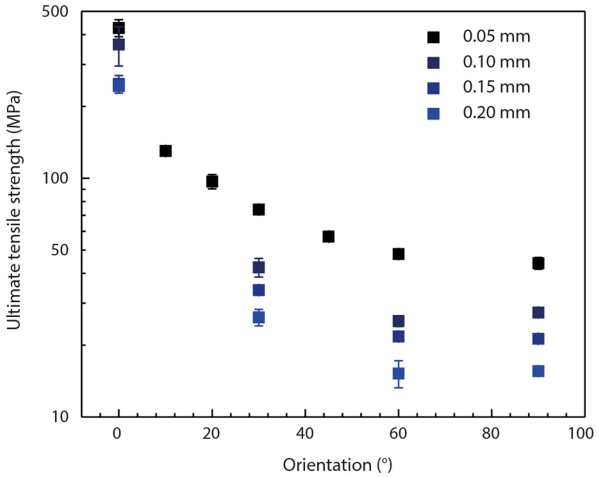

Extended Data Fig. 4 | Strength of LCP parts of different thicknesses as a function of print orientation. The observed decrease in tensile strength for increasing print orientations follows the decay in elastic modulus predicted from classical laminate theory (Fig. 3a). The lower strength at high orientation angles is also explained by a transition in failure mode from print filament fracture to interface fracture. Error bars indicate the standard deviation for 5–10 measurements at each data point; see Source Data for details.

© 2018 Springer Nature Limited. All rights reserved.

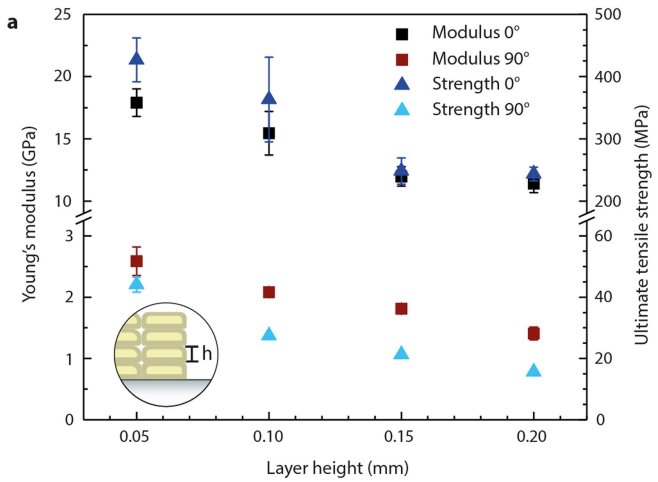

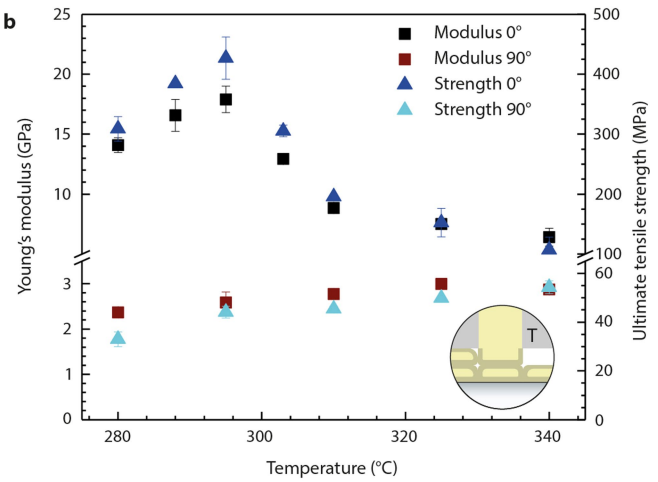

Extended Data Fig. 5 | Effect of print parameters on the Young's modulus of horizontally printed LCP parts. a, Tensile modulus and strength as a function of printed layer height. Lower layer heights lead to higher mechanical properties owing to the higher fraction of aligned skin relative to the material height. **b**, Tensile modulus and strength as a function of nozzle temperature (T_N). For temperatures higher than 300 °C, the tensile properties along the printing direction (0°) follows the behaviour observed for the Young's modulus of vertically printed filaments (Fig. 2g). The lower values obtained for the Young's modulus and strength at $T_N < 300$ °C probably result from poorer material flow and poorer print filament adhesion at lower nozzle temperatures. The tensile properties perpendicular to the print direction (90°) increase at higher temperatures, which inidicates an improved adhesion between hot printed filaments. Error bars indicate the standard deviation for 5–10 measurements at each data point; see Source Data for details.

© 2018 Springer Nature Limited. All rights reserved.

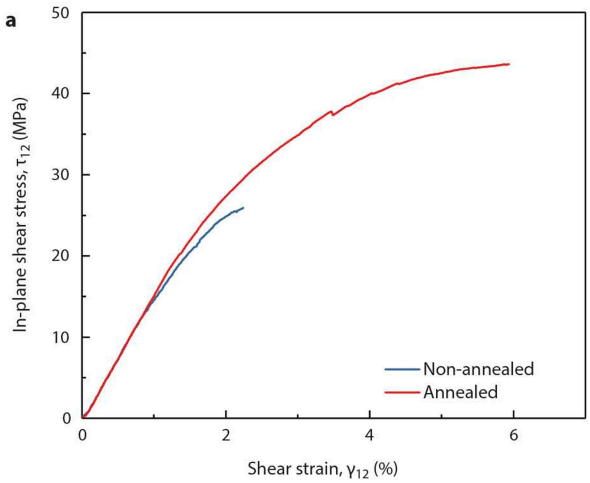

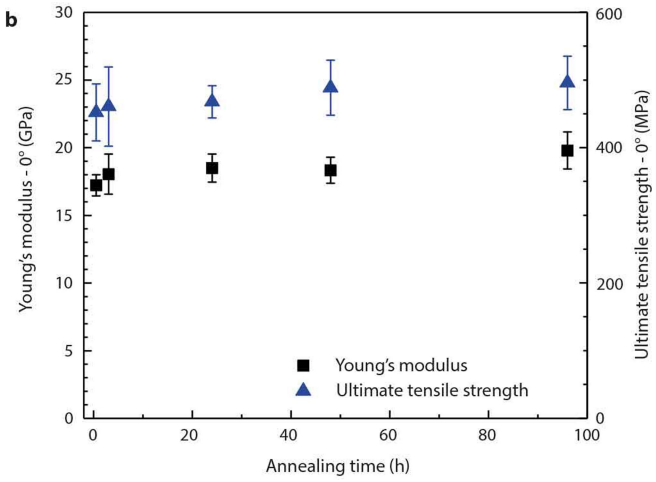

Extended Data Fig. 6 | Increased load transfer between filaments after annealing. a, Representative curve of shear stress versus strain shows that the shear strength of the LCP increases by 75% after thermal annealing for 96 h owing to the enhanced inter-filament adhesion. The shear strength data were obtained from ±45° tensile samples. **b**, The Young's modulus measured along the printing direction is found to slightly increase with longer annealing times. Error bars indicate the standard deviation for 5–10 measurements at each data point; see Source Data for details.

© 2018 Springer Nature Limited. All rights reserved.

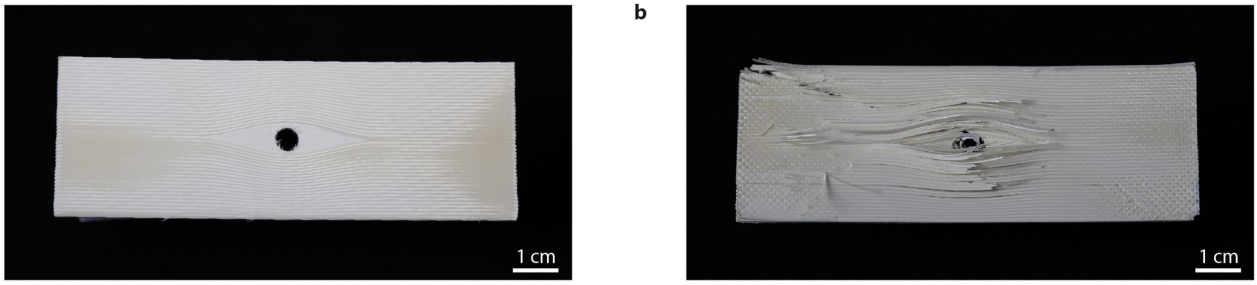

Extended Data Fig. 7 | Directional OHT sample. a, Print lines are guided around the hole, resembling a wood knot hole. The stress-shielded area next to the hole is reinforced with 90° filaments. **b**, The extensive damage to the same sample without catastrophic failure during tensile testing illustrates the high fracture toughness of the hierarchically structured architecture.

© 2018 Springer Nature Limited. All rights reserved.

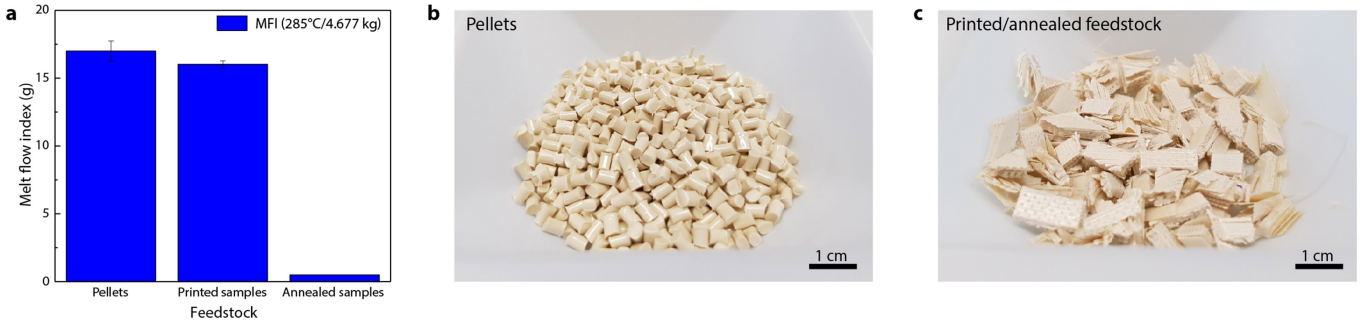

Extended Data Fig. 8 | Recyclability of printed LCP material. a, Melt flow index (MFI) of pristine pellets as well as recycled printed parts and recycled annealed printed parts (five measurements per material). The melt flow index quantifies the fluidity of the material at the indicated temperature and load. Higher indices indicate low viscosity. Non-annealed printed samples are readily recyclable owing to their high melt flow index. Although the higher molecular weight of annealed samples markedly reduces their fluidity at regular printing temperatures, this material is potentially recyclable if hydrolysis reactions are used to decrease its molecular weight and thus recover processability. Error bars indicate the standard deviation for 5 measurements at each data point; see Source Data for details. **b**, **c**, Examples of pellets (**b**) and recycled printed samples (**c**) as feedstock material.

© 2018 Springer Nature Limited. All rights reserved.

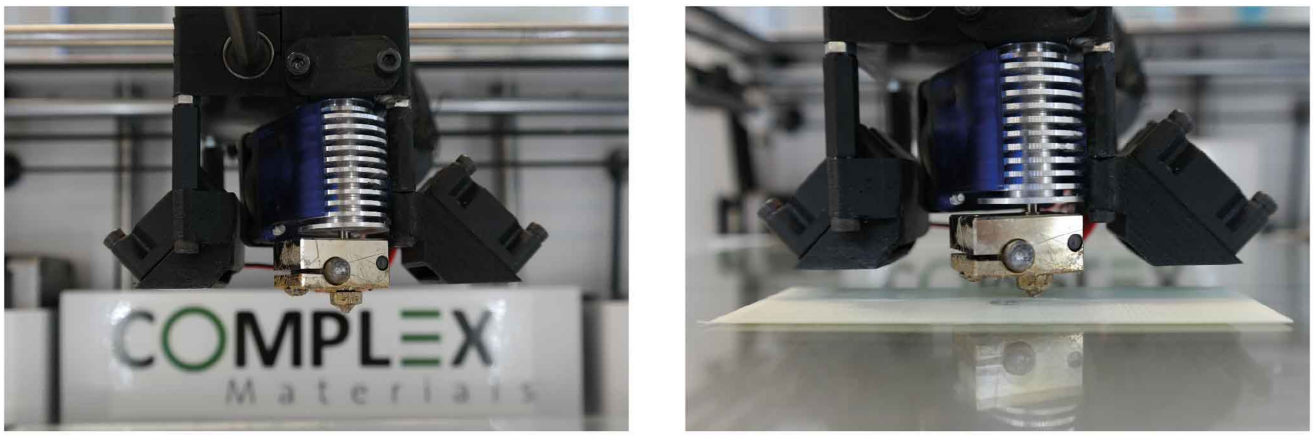

Extended Data Fig. 9 | Geared direct drive extruder with all-metal V6 hotend on an Ultimaker 2+.

© 2018 Springer Nature Limited. All rights reserved.

Extended Data Table 1 | Classical laminate theory parameters used for print filament layer heights between 0.05 mm and 0.20 mm

Layer height (mm)	0.05	0.10	0.15	0.20
E_{11} (GPa)	17.90	15.40	11.97	11.39
E_{22} (GPa)	2.58	2.08	1.81	1.40
G_{12} (GPa)	1.70	1.30	1.10	1.00
ν_{12}	0.57	0.57	0.57	0.57

© 2018 Springer Nature Limited. All rights reserved.